

Microwave amplification chain calibration in an axion haloscope via cavity-emitted radiation

Hsin Chang,¹ Han-Wen Liu,¹ Hien Thi Doan,² and Yung-Fu Chen^{1, a)}

¹⁾*Department of Physics, National Central University, Taoyuan City 320317, Taiwan*

²⁾*Institute of Physics, Academia Sinica, Taipei City 115201, Taiwan*

(Dated: 21 June 2024)

In an axion haloscope, the weak photon signal, theoretically converted from axions, is captured by a detection cavity. The amplification chain assists the signal receiver to read the signal from the cavity and requires accurate calibration. Typically, the readout line is calibrated using the Y-factor method, involving a switch that directs the signal from either the detection line or the calibration line. However, this switch introduces several disadvantages. In response, we propose a calibration method that eliminates the need for a switch. In this approach, the cavity temperature is decoupled to its incoming noise source and can be controlled, resulting in excess or deficiency of the noise spectrum near its resonance frequency. The experimental result shows that the amplification chain can be calibrated directly using the temperature-varied cavity-emitted radiation.

I. INTRODUCTION

In an axion¹⁻⁴ haloscope, the cavity immersed in a strong magnetic field is used as a detector⁵⁻⁷. The photons converted from the axions are stored in the cavity as the cavity resonance frequency f_c matches the photon frequency $f_a \equiv m_a c^2/h$, where c is the speed of light, m_a is the mass of axion, and h is the Planck constant. The photons in the cavity are captured via an antenna and acquired by a signal receiver. Besides the axion-converted photons, the cavity emits quantum or thermal noise as it is thermalized in an environment of temperature. The cavity should be kept cold to prevent thermal noise from contaminating the signal. Generally, a dilution refrigerator is used to host the cavity⁸⁻¹² as it provides a continuous cooling for massive materials down to the order of 10 mK. Moreover, the axion-to-photon converted signal power is extremely weak, below the order of 10^{-22} W¹³⁻²⁷. Various types of readout approaches are being considered for capturing the conversion signals. Compared to single-photon detectors, a linear amplification chain shows benefits in the detection range of $f_a \sim 1-10$ GHz²⁸. The sensitivity of the detector can be determined once the system noise and the emitted power at the cavity are known from the reading power of the signal receiver. To achieve this, calibrating the gain of the amplification chain is essential. The added noise of the amplification chain is also measured and indicates the performance of the system.

To calibrate the linear amplification chain, a source that emits a known and adjustable power P_s is required. During the calibration process, the reading power of the signal receiver P_r depends on P_s linearly. The slope and the intersection with the y-axis of P_r versus P_s give the gain and added noise of the amplification chain, respectively. Typically, a Y-factor method, as denoted in

Fig. 1(a), is used^{9,29,30}. For gain calibration, the switch directs the readout to the black-body radiation source (BS), whose emitted power is adjusted and measured by the heater and thermometer, respectively. BS serves the source of P_s and is used to calibrate the gain from BS to the signal receiver. For axion detection, the switch connects the amplification chain to the cavity. An antenna marked in orange is inserted into a microwave (MW) cavity as a probe. The emitted power at the cavity is inferred via the calibration. However, the detection and calibration have different transmission paths before the switch. The different attenuation of cables between the paths leads to the calibration results being less accurate. Besides, the mixing plate will be heated while the switch is operating. This causes extra waiting time during the axion search. Also, the connection loss of the switch does not promise to be consistent in every operation.

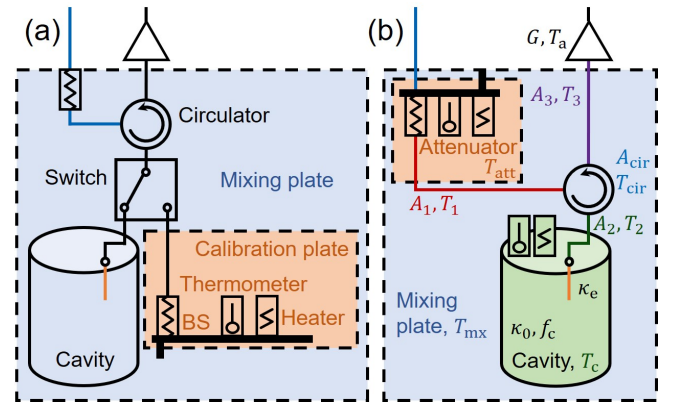


FIG. 1. Axion haloscope setup. (a) Y-factor calibration setup. A cryogenic switch connects the readout chain to the cavity or the black-body radiation source. (b) Cavity-emitted radiation calibration setup. The amplification chain is calibrated directly by cavity-emitted radiation.

To avoid the need for switches, different calibration methods have been developed^{31,32}. Here, we propose us-

^{a)}Correspondence to: yfuchen@ncu.edu.tw

ing the cavity as a calibration source so that the detection path is directly calibrated. Since no switch is involved, the problems in the Y-factor method are mitigated. The gain obtained in the calibration process can be applied to the axion search without the concerns mentioned above. A model is introduced to derive the noise spectrum from a cavity that is not thermalized with its incoming noise source. The losses of MW components are considered in the model to make the calibration results more accurate. The formalism agreed with the experimental data from a hot cavity of $f_c \approx 5$ GHz. The result indicates that a hot cavity can manifest its temperature through its noise spectrum near the resonance frequency, and the cavity-emitted radiation is a reliable noise source for amplification chain calibration.

II. CAVITY-EMITTED RADIATION CALIBRATION

Past experiments have indicated that a hot cavity emits an excess noise power near its resonance^{10,33}. The width of the excess power is about the cavity bandwidth. The phenomenon was explained by Ref.³³⁻³⁵: The entire noise spectrum is determined by the incoming noise reflected by the cavity and the thermal noise emitted by the cavity at an elevated temperature. The previous studies on cavity-emitted radiation inspire us to directly use the cavity as the calibration source. We propose an axion haloscope setup to avoid the disadvantages of Y-factor calibration configuration from having a switch. As depicted in Fig. 1(b), the cavity is inserted by an antenna and connected to an attenuator as an incoming noise source. The temperature of the attenuator and the cavity are denoted as T_{att} and T_c , respectively. The circulator allows the measurement of the reflection scattering parameter (S-parameter) by injecting a continuous wave from the blue cable. The scattering characteristics of the cavity are governed by intrinsic loss rate κ_0 , external coupling rate κ_e to the antenna, and the cavity resonance frequency f_c . Cable 1, 2, and 3 are marked in red, green, and purple with loss A_1 , A_2 , and A_3 , respectively. The cavity-emitted radiation is added a noise T_a and amplified with gain G via the amplifier. To simplify the discussion, we first focus on the cavity-emitted spectrum under the assumption of cables with no loss, i.e., $A_1 = A_2 = A_3 = 1$, highlighting its potential as a calibration source. Then, the effect of cable loss is investigated to provide a more accurate representation of the practical setup. Moreover, since the cables at both ends contact with different temperatures, a linear temperature distribution of the cables, T_1 , T_2 , and T_3 , has also been considered.

As indicated in Fig. 1(b), the cavity-emitted radiation consists of noise from the attenuator and the cavity. Thus, the cavity-emitted radiation power under the cables without loss is given by Ref.^{33,35},

$$P_c(f) = \left(|S_r|^2 \tilde{T}_{\text{att}} + |S_t|^2 \tilde{T}_c \right) k_B B, \quad (1)$$

where

$$S_r(f) = \frac{\kappa_0 - \kappa_e + 2i\Delta}{\kappa_0 + \kappa_e + 2i\Delta}, \quad (2a)$$

$$S_t(f) = \frac{2\sqrt{\kappa_0\kappa_e}}{\kappa_0 + \kappa_e + 2i\Delta} \quad (2b)$$

is the reflection scattering factor of the antenna and the transmission factor from the cavity to the antenna, respectively, k_B is Boltzmann constant, B is the frequency bandwidth, $\Delta = f - f_c$ is the frequency detuning from f_c , and f is the frequency. The effective noise temperature $\tilde{T}_x = \tilde{T}(T_x)$ is expressed as

$$\tilde{T}(T_x) = \frac{hf}{k_B} \left(\frac{1}{e^{hf/k_B T_x} - 1} + \frac{1}{2} \right) \quad (3)$$

for the physical temperature T_x , x stands for various physical objects. In Eq. 1, $|S_r|^2$ and $|S_t|^2$ are obtained by S-parameter measurement, \tilde{T}_{att} and \tilde{T}_c are determined by Eq. 3. The known and adjustable P_c provides source power, P_s , and the reading power after amplification is

$$P_r(f) = G(P_c + k_B T_a B). \quad (4)$$

The spectrum of P_r follows that of P_c , and exhibits a peak near f_c when $T_{\text{att}} < T_c$, and a dip when $T_{\text{att}} > T_c$. When $T_{\text{att}} = T_c$, it corresponds to white noise since $|S_r|^2 + |S_t|^2 = 1$.

The discussion up to this point has considered lossless MW components, whereas cables and circulators typically exhibit attenuation. We first look into the effect of loss on the circulator. Consider the noise \tilde{T}_{att} transmitted through the circulator with a loss A_{cir} and temperature T_{cir} . Based on the fluctuation-dissipation theorem, the output consists of the attenuated \tilde{T}_{att} and the additional noise introduced by the circulator, as described by $A_{\text{cir}}\tilde{T}_{\text{att}} + (1 - A_{\text{cir}})\tilde{T}_{\text{cir}}$. For the noise generated by cable 1, the cable temperature as a function of space, $T_1 = T_1(x)$, should be considered. The spatial coordinate of the cable x is defined from the attenuator x_{att} to the circulator x_{cir} , with corresponding temperature T_{att} and T_{cir} . The generated noise of the cable is given as the integral of effective noise temperature at x attenuated by the cable with length $|x_{\text{cir}} - x|$ with respect to x , that is

$$\tilde{T}_1^* = \int_{x_{\text{att}}}^{x_{\text{cir}}} \tilde{T}_1(x) A_1(x) \frac{dx}{l}, \quad (5)$$

where $\tilde{T}_1(x) = \tilde{T}[T_1(x)]$, $T_1(x) = T_{\text{att}} + \frac{x - x_{\text{att}}}{x_{\text{cir}} - x_{\text{att}}}(T_{\text{cir}} - T_{\text{att}})$ due to the assumption of constant thermal conductivity in the cable, $A_1(x) = e^{-|x_{\text{cir}} - x|/l}$, and l represents the attenuation length. The total loss of cable 1 is expressed as $A_1 = e^{-|x_{\text{cir}} - x_{\text{att}}|/l}$. This applies to all cables.

Figure 2 shows the integral of Eq. 5 for $f = 5$ GHz at $A_1 = 1, 0.8, 0.7$, and 0. The y-axis in (a) and (b) are set in the same range for comparison. Figure 2(a) illustrates \tilde{T}_1^* as a function of T_{cir} for $T_{\text{att}} = 12$ mK, which is much lower than cross-over temperature $hf/2k_B = 120$ mK. A

lossless cable, as $A_1 = 1$ shown by the blue line, does not generate noise. As the attenuation increases (smaller A_1), \tilde{T}_1^* increases. The inset shows that the cable becomes a thermal insulator when $A_1 = 0$, and \tilde{T}_1^* is independent of T_{att} and equals \tilde{T}_{mx} . Figure 2(b) depicts \tilde{T}_1^* as a function of T_{att} with the condition of $T_{\text{mx}} = 12$ mK. Since $A_1(x)$ assigns a weight to each $\tilde{T}_1(x)$, \tilde{T}_1^* is more relevant to T_{cir} . It should be noted that the generated noise depends on the direction of the signal path.

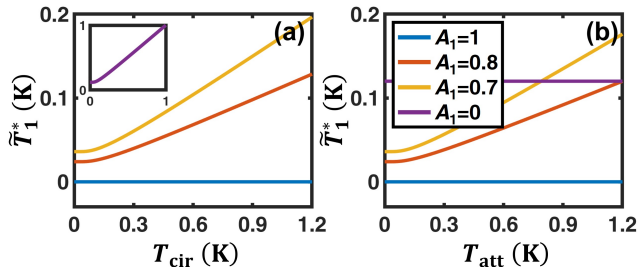


FIG. 2. The generated noise from the cable \tilde{T}_1^* . The plot is based on Eq. 5 where $f = 5$ GHz, and A_1 is set at 1, 0.8, 0.7, and 0. (a) \tilde{T}_1^* as a function of T_{cir} where T_{att} is fixed at 12 mK. (b) \tilde{T}_1^* as a function of T_{att} for $T_{\text{cir}} = 12$ mK.

Considering the losses of the MW components, the incoming noise to the cavity should include not only the noise from the attenuator but also the generated noises from cable 1, circulator, and cable 2, and can be expressed to

$$T_{\text{in}} = A_2 \left[A_{\text{cir}} \left(A_1 \tilde{T}_{\text{att}} + \tilde{T}_1^* \right) + (1 - A_{\text{cir}}) \tilde{T}_{\text{cir}} \right] + \tilde{T}_2^*. \quad (6)$$

By collecting the losses, $A_{\text{in}} = A_2 A_{\text{cir}} A_1$, and the generated noises of MW components, $\hat{T}_{\text{in}} = A_2 A_{\text{cir}} \tilde{T}_1^* + A_2 (1 - A_{\text{cir}}) \tilde{T}_{\text{cir}} + \tilde{T}_2^*$, T_{in} is rearranged to

$$T_{\text{in}} = A_{\text{in}} \tilde{T}_{\text{att}} + \hat{T}_{\text{in}}. \quad (7)$$

The cavity-emitted radiation power is modified as

$$P_c(f) = \left(|S_r|^2 T_{\text{in}} + |S_t|^2 \tilde{T}_c \right) k_B B. \quad (8)$$

For the calibration, cable 2, circulator, and cable 3 should be included in the amplification chain. The losses and generated noises of MW components before the first-stage amplifier are collected into $A_r = A_3 A_{\text{cir}} A_2$ and $\hat{T}_r = A_3 A_{\text{cir}} \tilde{T}_2^{*-} + A_3 (1 - A_{\text{cir}}) \tilde{T}_{\text{mx}} + \tilde{T}_3^*$. \tilde{T}_2^{*-} denotes the noise generated by cable 2 in the direction outward from the cavity. The reading power after amplification is

$$\begin{aligned} P_r(f) &= G \left(A_r P_c + k_B \hat{T}_r B + k_B T_a B \right) \\ &= G' \left(P_c + k_B T_a' B \right). \end{aligned} \quad (9)$$

An effective gain, $G' = G A_r$, and effective added noise, $T_a' = (\hat{T}_r + T_a) / A_r$, reveals that the signal is degraded

by a factor of A_r , while the noise is increased by a factor of $1/A_r$. In cavity-emitted radiation calibration, P_c acts as the calibration source P_s . The calibration gives G' , which is used for sensitivity determination and noise performance during axion search. The experimental results show the added noise included \hat{T}_r can be represented by one fitting parameter T_a' .

III. EXPERIMENTAL SETUP

The setup of cavity-emitted radiation calibration is demonstrated in Fig. 1(b), which comprises the attenuator plate, marked in orange, and the cavity. The attenuator plate and the cavity are thermal-anchored via two stainless steel pillars to the mixing plate. The poor thermal conductance of pillars ensures that the temperature of the mixing plate will not be significantly affected during the heating process. Thus, T_{att} and T_c can be controlled independently by the resistive heaters and RuO_2 thermometers. The attenuator is not only used as a radiation source but also reduces thermal noise from the input line (cable in blue). This ensures that the incoming noise to the cavity is mainly contributed by the attenuator. Cable 1 and 2 are CryoCoax-BCB012 superconducting cables with 40 cm and 53.5 cm long, respectively, to reduce the attenuation on \tilde{T}_{att} . The LNF-CIISISC4_8A circulator propagates the outgoing field from the cavity to the amplification chain and prevents thermal radiation from the amplifier from being transmitted back to the cavity. The circulator also allows reflection spectroscopy measurement. The amplification chain is composed of an LNF-LNC4_8C low-noise high-electron-mobility-transistor amplifier on the 4K plate and a three-stage Mini-Circuits ZX60-83LN-S+ room-temperature post-amplifier (not shown in the figure). The power is analyzed through the fast Fourier transformation with bandwidth $B = 1$ kHz and a three-minute integration time by the NI PXIe-5644R vector signal transceiver.

IV. EXPERIMENTAL RESULTS

To demonstrate our calibration method, the cavity parameters are first obtained through the reflection spectroscopy measurement. Then, the cavity-emitted spectrum is taken under various T_{att} and T_c . An asymmetric spectrum for P_r is observed in our setup, presumably due to the nonuniform response of the readout chain^{36,37}. Typically, this nonuniform frequency response in halo-scope experiments is removed by digital filters, such as the Savitzky-Golay (SG) filter or Padé filter, when processing the data^{33,38,39}. In this work, the frequency dependence is distinguished from the fitting of Eq. 9. Theoretically, both T_a' and G' as a function of frequency lead to a nonuniform behavior. However, T_a' involves fewer MW components and typically behaves as a constant within a

sufficiently small measurement span. Therefore, We take $G' = G'(f)$ into account. To determine the frequency dependence, the fitting is first applied by five fitting parameters, \bar{G}' , T'_a , A_1 , A_{cir} , and A_2 , where \bar{G}' is assumed to be frequency independent. The fitting result of \bar{G}' corresponds to the averaged gain in the measurement frequency span. The frequency dependence is derived from the ratio between the data and the fitting curve.

A. Reflection spectroscopy measurement

The factors $|S_r|^2$ and $|S_t|^2$ in Eq. 8 are related to the cavity characteristics, κ_0 , κ_e , and f_c . The reflection spectroscopy measurement is sufficient to determine all the characteristic parameters. The reflection spectroscopy of a cavity coupled with an external antenna is given by Eq. 2a. In Fig. 3, the fitting of amplitude $|A|^2$ and phase ϕ give the cavity parameters $\kappa_0 = 432$ kHz, $\kappa_e = 149$ kHz and $f_c = 4.944458$ GHz. Since far-detuning approximation brings $|S_r|^2$ to 1, the baseline offset of $|A|^2$ is due to the attenuation of the input line and amplification of the readout line.

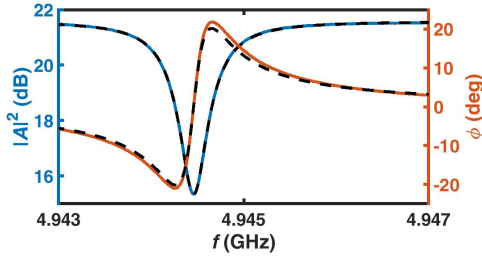


FIG. 3. The cavity reflection scattering measurement. The solid lines are the experimental data. The dashed line is the fitting with Eq. 2a and gives $\kappa_0 = 432$ kHz, $\kappa_e = 149$ kHz and $f_c = 4.944458$ GHz.

B. Cavity-emitted radiation

Fig. 4 shows the cavity-emitted spectrum under various combinations of T_{att} and T_c . The temperatures monitored by thermometers are listed in Tab. IV B. $T_{\text{cir}} = T_{\text{mx}}$ is assumed because the circulator attaches to the mixing plate. The measured spectrum, as depicted by the solid curve, shows asymmetric shapes caused by $G'(f)$. By fitting eight data in Tab. IV B to Eq. 9, we obtain $\bar{G}' = 93.07$ dB, $T'_a = 5.28$ K, $A_1 = 1.00$, $A_{\text{cir}} = 0.77$, and $A_2 = 0.94$. The agreement between the data and the fitting curves is very good for all the data sets. The minor discrepancy is assumed to be due to the frequency dependence of the readout line gain, which is expressed as $G'(f) = r(f)\bar{G}'$. The ratio $r(f)$ is determined by averaging the ratio between the data and the fitting of eight data curves and smoothing the averaged result via the SG filter. Figure 5(a) plots $r(f)$ and reveals

that the variation of gain in frequency is 0.37%. Besides, the ratios of the eight data curves to their corresponding fitting curves have similar shapes but drift by 0.13% over a three-hour experimental time. The data normalized by $r(f)$ are plotted in Fig. 5(b) and (c). Note that the green curve is taken while $T_c \approx T_{\text{att}}$ but exhibits a peak spectrum. If the incoming noise generated from MW components is only considered for a single cable with temperature distributed from T_{att} to T_c , one would expect a flat spectrum, which is not observed in the measurement. A colder T_{mx} results in a smaller T_{in} and thus a smaller off-resonance background, which in turn leads to a peak near the resonance. Equation 9 includes this effect and fits well in this scenario. Besides, the cavity emits a flat spectrum while $T_{\text{att}} \approx T_c \approx T_{\text{mx}}$. Under this condition, the nonuniform spectrum observed by the signal receiver directly reveals the frequency dependence of readout line gain.

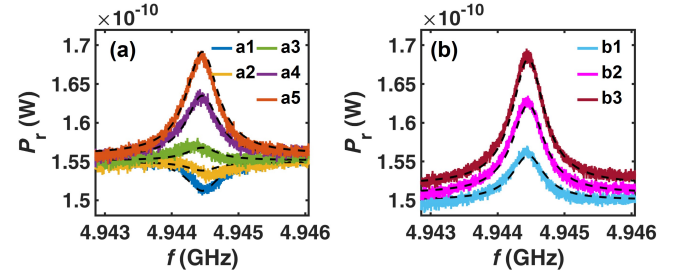


FIG. 4. The reading power of cavity-emitted spectrum. The monitored temperatures are depicted in Tab. IV B. The solid curves are the measurement, and the dashed curves are the fitting to Eq. 9. (a) The data collection with $T_{\text{att}} \approx 340$ mK, and T_c is adjusted from below to above T_{att} . (b) The data collection with low T_{att} and heated T_c .

Curve	T_{att}	T_c	T_{mx}	Curve	T_{att}	T_c	T_c
a1	342	78	23	b1	83	348	28
a2	332	202	25	b2	108	646	44
a3	336	338	30	b3	147	910	63
a4	339	648	46				
a5	341	909	63				

TABLE I. The readings of thermometers on the attenuator plate, the cavity, and the mixing plate during the data collection in Fig. 4. The temperatures are in units of mK.

To verify the fitting results, the estimated losses are compared to the specifications provided by manufacturers. As the instrument models introduced in Sec. III, the losses of the cables are $A_1 = 0.96$ and $A_2 = 0.94$, which are close to the fitting results. However, the insertion loss of the circulator, $A_{\text{cir}} = 0.96$, differs from the fitting. To examine the effect of this discrepancy on the estimation of \bar{G}' , we perform the fitting by fixing the losses to the values from the specifications. The results, as shown in Fig. 5(d)-(f), give $\bar{G}' = 92.94$ dB and $T'_a = 5.43$ K. Here, \bar{G}' differs by 3% from the aforementioned fitting result, where all losses are considered as free parameters.

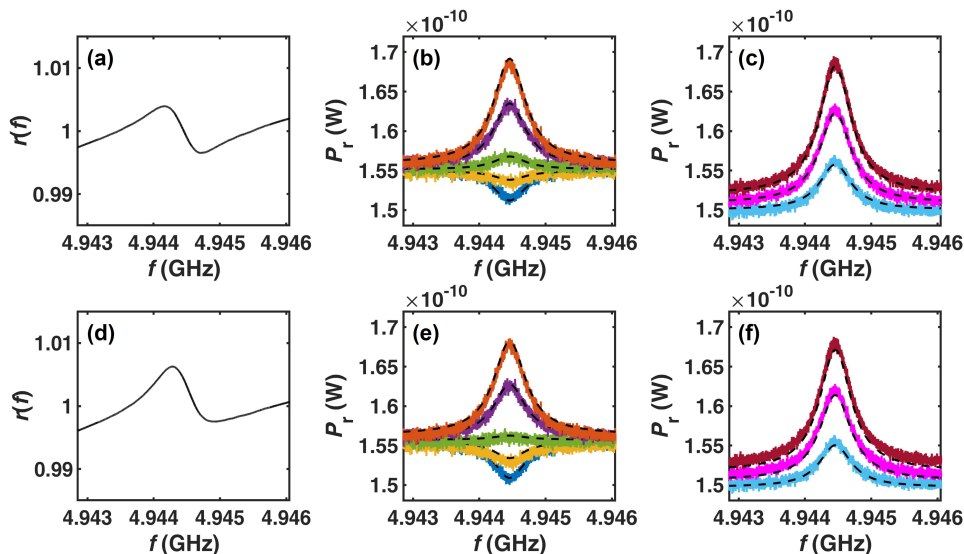


FIG. 5. The fitting results and the normalized data with different considerations on losses. (a)-(c) The fitting where the losses are considered as free fitting parameters. $r(f) = G'(f)/\bar{G}'$ is determined from the data fitting. The data in Fig. 4 after normalized with respect to $r(f)$, as depicted by solid curves. The dashed curves are the fitting to Eq. 9. (d)-(f) The fitting with the losses introduced from the specifications of the manufacturer.

Because the radiation from the attenuator is the source to calibrate A_{cir} , systematic errors in the thermometer on the attenuator plate could cause inconsistency in A_{cir} . Besides, the fittings have some residual disagreement with the data at off-resonance, which is mostly contributed by T_{in} according to Eq. 8. These imply that the estimation for T_{att} is inaccurate or the model for noise generated by the MW components is incomplete, but the effect is small enough to give a good approximation to determine \bar{G}' .

V. CONCLUSION

In this work, We modify the haloscope setup by directly using the cavity as the calibration source, enabling the calibration and detection to share the same path. The absence of a switch eliminates concerns of different attenuation among coaxial cables, heating, and inconsistent connection from the operating switch. Additionally, the frequency dependence of the readout line gain can be identified by the analysis of the measured cavity-emitted spectrum. Furthermore, the impact of lossy cables has been studied, and the experimental results are in agreement. The consideration of losses for the incoming noise offers a more accurate description of the realistic behavior of the cavity-emitted spectrum. The cavity-emitted radiation method has been properly understood and provides a more reliable calibration process.

VI. ACKNOWLEDGMENTS

We are grateful to Yuan-Hann Chang for their helpful discussions. The work is strongly supported by the Taiwan Axion Search Experiment with Haloscope (TASEH) collaboration. The work was supported by the National Science and Technology Council in Taiwan under grant No. NSTC 111-2123-M-001-004 and No. NSTC 112-2123-M-001-001.

- ¹R. D. Peccei and H. R. Quinn, *Physical Review Letters* **38**, 1440 (1977).
- ²R. D. Peccei and H. R. Quinn, *Physical Review D* **16**, 1791 (1977).
- ³S. Weinberg, *Physical Review Letters* **40**, 223 (1978).
- ⁴F. Wilczek, *Physical Review Letters* **40**, 279 (1978).
- ⁵P. Sikivie, *Physical Review Letters* **51**, 1415 (1983).
- ⁶P. Sikivie, *Physical Review D* **32**, 2988 (1985).
- ⁷P. Sikivie, *Reviews of Modern Physics* **93**, 015004 (2021).
- ⁸H. Chang, J. Y. Chang, Y. C. Chang, Y. H. Chang, Y. H. Chang, C. H. Chen, ... and TASEH Collaboration, *Physical Review Letters* **129**(11), 111802 (2022).
- ⁹H. Chang, J. Y. Chang, Y. C. Chang, Y. H. Chang, Y. H. Chang, C. H. Chen, ... and TASEH Collaboration, *Review of Scientific Instruments* **93**(8), 084501 (2022).
- ¹⁰S. Al Kenany, M. Anil, K. Backes, B. Brubaker, S. Cahn, G. Carosi, ... and L. Zhong, *Nuclear Instruments and Methods in Physics Research Section A: Accelerators, Spectrometers, Detectors and Associated Equipment* **854**, 11 (2017).
- ¹¹R. Khawwaja, D. Bowring, A. Chou, A. Sonnenschein, W. Wester, D. Mitchell, ... and G. C. Hilton, *Review of Scientific Instruments* **92**, 124502 (2021).
- ¹²J. Choi, S. Ahn, B. Ko, S. Lee, and Y. K. Semertzidis, *Nuclear Instruments and Methods in Physics Research Section A: Accelerators, Spectrometers, Detectors and Associated Equipment* **1013**, 165667 (2021).
- ¹³S. Borsanyi, Z. Fodor, J. Guenther, K.-H. Kampert, S. D. Katz, T. Kawanai, T. G. Kovacs, S.W. Mages, A. Pasztor, F. Pittler, J.

- Redondo, A. Ringwald, and K. K. Szabo, *Nature (London)* **539**, 69 (2016).
- ¹⁴M. Dine, P. Draper, L. Stephenson-Haskins, and D. Xu, *Physical Review D* **96**, 095001 (2017).
- ¹⁵T. Hiramatsu, M. Kawasaki, T. Sekiguchi, M. Yamaguchi, and J. Yokoyama, *Physical Review D* **83**, 123531 (2011).
- ¹⁶M. Kawasaki, K. Saikawa, and T. Sekiguchi, *Physical Review D* **91**, 065014 (2015).
- ¹⁷E. Berkowitz, M. I. Buchoff, and E. Rinaldi, *Physical Review D* **92**, 034507 (2015).
- ¹⁸P. Petreczky, H.-P. Schadler, and S. Sharma, *Physical Review B* **762**, 498 (2016).
- ¹⁹G. Ballesteros, J. Redondo, A. Ringwald, and C. Tamarit, *Physical Review Letters* **118**, 071802 (2017).
- ²⁰M. Buschmann, J.W. Foster, and B. R. Safdi, *Physical Review Letters* **124**, 161103 (2020).
- ²¹C. Hagmann, D. Kinion, W. Stoeffl, K. Van Bibber, E. Daw, H. Peng, ... and N. A. Golubev, *Physical Review Letters* **80**(10), 2043 (1998).
- ²²S. J. Asztalos, G. Carosi, C. Hagmann, D. Kinion, K. Van Bibber, M. Hotz, ... and J. Clarke, *Physical review letters* **104**(4), 041301 (2010).
- ²³C. Bartram, T. Braine, E. Burns, R. Cervantes, N. Crisosto, N. Du, ... and ADMX Collaboration. *Physical review letters* **127**(26), 261803 (2021).
- ²⁴B. M. Brubaker, L. Zhong, Y. V. Gurevich, S. B. Cahn, S. K. Lamoreaux, M. Simanovskaia, ... and G. Carosi, *Physical review letters* **118**(6), 061302 (2017).
- ²⁵L. Zhong, S. Al Kenany, K. M. Backes, B. M. Brubaker, S. B. Cahn, G. Carosi, ... and K. Van Bibber, *Physical Review D* **97**(9), 092001 (2018).
- ²⁶K. M. Backes, D. A. Palken, S. A. Kenany, B. M. Brubaker, S. B. Cahn, A. Droster, ... and H. Wang, *Nature* **590**(7845), 238-242 (2021).
- ²⁷O. Kwon, D. Lee, W. Chung, D. Ahn, H. Byun, F. Caspers, ... and Y. K. Semertzidis, *Physical Review Letters* **126**(19), 191802 (2021).
- ²⁸S. K. Lamoreaux, K. A. van Bibber, K. W. Lehnert, and G. Carosi, *Physical Review D* **88**(3), 035020 (2013)
- ²⁹D. Alesini, C. Braggio, G. Carugno, N. Crescini, D. D'Agostino, D. Di Gioacchino, ... and S. Tocci, *Physical Review D* **99**(10), 101101 (2019).
- ³⁰Y. Lee, B. Yang, H. Yoon, M. Ahn, H. Park, B. Min, ... and J. Yoo, *Physical review letters* **128**(24), 241805 (2022).
- ³¹C. Braggio, G. Cappelli, G. Carugno, N. Crescini, R. Di Vora, M. Esposito, ... and G. Ruoso, *Review of Scientific Instruments* **93**(9), 094701, (2022).
- ³²N. Crescini, D. Alesini, C. Braggio, G. Carugno, D. D'Agostino, D. Di Gioacchino, ... and QUAX Collaboration, *Physical Review Letters* **124**(17), 171801 (2020).
- ³³H. Chang, J. Y. Chang, Y. C. Chang, Y. H. Chang, Y. H. Chang, C. H. Chen, ... and TASEH Collaboration, *Physical Review D* **106**(5), 052002 (2022).
- ³⁴D. Alesini, C. Braggio, G. Carugno, N. Crescini, D. D'Agostino, D. Di Gioacchino, ... and S. Tocci, *Physical Review D* **103**, 102004 (2021).
- ³⁵K. Wurtz, B. M. Brubaker, Y. Jiang, E. P. Ruddy, D. A. Palken, and K. W. Lehnert, *Physical Review X Quantum* **2**(4), 040350 (2021).
- ³⁶S. Asztalos, E. Daw, H. Peng, L. Rosenberg, C. Hagmann, D. Kinion, ... Bradley, R. F., *Physical Review D* **64**, 092003 (2001).
- ³⁷S. Lee, S. Ahn, J. Choi, B. R. Ko, and Y. K. Semertzidis, *Physical review letters* **124**, 101802 (2020).
- ³⁸B. Brubaker, L. Zhong, S. Lamoreaux, K. Lehnert, and K. van Bibber, *Physical Review D* **96**, 123008 (2017).
- ³⁹C. Bartram, T. Braine, R. Cervantes, N. Crisosto, N. Du, G. Leum, ... ADMX Collaboration, *Physical Review D* **103**, 032002 (2021).